A Step-Up Bidirectional Series Resonant DC/DC Converter Using a Continuous Current Mode

Federico Martin Ibanez, Jose Martin Echeverria, Javier Vadillo, and Luis Fontan, *Senior Member, IEEE*

***Abstract*—This paper presents the analysis and design of a novel technique that allows the conventional series resonant dc/dc converter (SRC) to work as a step-up and step-down converter. This is useful in bidirectional dc/dc converters where one port is attached to a fixed voltage dc line, e.g., a 360-V dc line, and the other port is attached to an energy storage device such as a bank of supercapacitors or batteries. Every converter that works in this scenario requires step-up and step-down modes to transfer energy from one port to the other. The paper presents the SRC as an alternative to the well-known dual active bridge (DAB). The dc analysis is detailed to demonstrate the step-up capability. In addition, the ac analysis is presented. Experimental results from a 6-kW prototype validate the theoretical analysis. The results indicate that this technique achieves better efficiency compared to the phase-shift DAB in a wide power range, from heavy to light loads. The main reason for this is that the converter works with smaller currents than the DAB at light loads.**

***Index Terms*—DC/DC converter, resonant converter, supercapacitor (SC).**

NOMENCLATURE

N	Transformer turns ratio.
M	Voltage conversion ratio, $V_{\rm OUT}/V_{\rm IN.}$.
M_{12}, M_{21}	M defined as: $M_{21} = V_{\rm 2DC}/V_{\rm 1DC}$ and $M_{12} = V_{\rm 1DC}/V_{\rm 2DC}$.
m, m_{12}, m_{21}	Normalized voltage conversion ratio, without considering the transformer turns ratio (n), $m = V_{\rm OUT}/(n * V_{\rm IN})$. $m_{21} = V_{\rm 2DC}/(n * V_{\rm 1DC})$ and $m_{12} = V_{\rm 1DC}/V_{\rm 2DC}$.
$X_{\rm min}, X_{\rm MAX}$	Minimum and maximum value of X where X can be m_{12} or m_{21}.
$V_{\rm 1DC}, V_{\rm 2DC}$	Low- and high-voltage side of the converter, respectively.
V_1, V_2	Equivalent source voltages use for the simplified circuit that excite the resonant branch.
$V_{\rm IN}, V_{\rm OUT}$	DC input and output voltage for the analysis, $V_{\rm IN} = n \cdot V_{\rm 1DC}$ and $V_{\rm OUT} = V_{\rm 2DC}$.
i_L, i_T, v_C	Inductor (L_R) current, low side transformer (XFRM) current, capacitor (C_R) voltage.
i_R	Rectified current.
R	Load resistor.
Z_0	Characteristic impedance of the resonant branch, $Z_0 = (L_R/C_R)^{1/2}$.
k	Attenuator factor, $k = R_{\rm LOSS}/(2L_R)$.
r	Normalized load resistor R/Z_0.
t_1, t_2, t_3	Time intervals where V_1 and V_2 remain constant.
V_T, M_T	$V_T = V_1$–V_2 and $M_T = V_T/V_{\rm IN.}$
v_{C1}	Initial C_R voltage.
ϕ_n	Initial phase of the n time interval.
$X_{(n)}$	X function for the n time interval.
$\omega_0, \omega_{S,f0,f_S}$	Resonant and switching frequency (rad/s) and (Hz), respectively.
T_0, T_S	Resonant and switching period (s).
F	Normalized switching frequency $\omega_S/\omega_{0.}$.
m_C, j_L	Normalized capacitor voltage is $m_C = v_C/V_{\rm IN}$ and normalized inductor current is $j_L = i_L \cdot Z_0/V_{\rm IN}$.
$H_{(n)}$	Radius for n-time interval in the m_C, j_L plane.
γ, α, β, ϕ	Angles for t_1, t_2 and t_3 time intervals in the m_C, j_L plane and ϕ is the initial angle.
$I_{\rm OUT}$	DC output current $V_{\rm OUT}/R$.
Q	Quality factor, $Q = 1/r$.
$\boldsymbol{A_n}, \boldsymbol{b_n}, \boldsymbol{c_n}$	State-space model for the nth time interval.
$\boldsymbol{A}, \boldsymbol{B}, \boldsymbol{k_1}, k_2, \boldsymbol{h}, \boldsymbol{d_S}, k_S$	Auxiliary matrixes, vectors, and constant for the small-perturbation model functions of the components of the circuit.
$v_{\rm IN}, v_{\rm OUT}$	Input and output voltage (DC+AC).
$\overline{x}, \hat{x}$	Period averaged and perturbation of x variable.

Manuscript received November 25, 2013; revised February 4, 2014; accepted April 13, 2014. Date of publication April 17, 2014; date of current version October 15, 2014. Recommended for publication by Associate Editor T. Shimizu.

The authors are with the CEIT, Electronics and Communications, Manuel de Lardizabal, San Sebastian 20009, Spain (e-mail: fmibanez@ceit.es; jmecheverria@ceit.es; jvadillo@ceit.es; fontan@ceit.es).

Color versions of one or more of the figures in this paper are available online at http://ieeexplore.ieee.org.

Digital Object Identifier 10.1109/TPEL.2014.2318202

I. INTRODUCTION

ENERGY storage systems (ESS) are being used more and more frequently because of the increase in the development of renewable energies like solar and wind energies. Commonly, these kinds of energy sources require an ESS that accumulates energy that can be consumed when it is needed. There are several types of ESS, such as batteries, supercapacitors (SCs) [1],

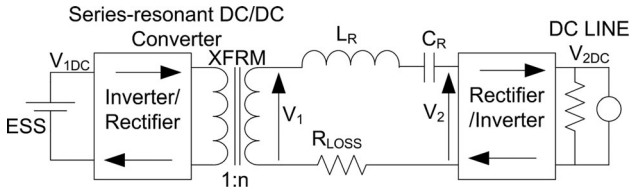

Fig. 1. General bidirectional SRC dc/dc converter diagram.

fuel cells, etc. SCs combined with batteries can increase the discharge life of a battery by smoothing its discharge current [2]–[4]. This not only means that less heat is produced by the battery, but also a greater charge can be extracted from the battery. However, because the output voltage in SCs is linearly dependent on its charge, a bidirectional dc/dc converter that attains a constant voltage at one port (output port) and allows fluctuations at the other port (input or SC port) must be introduced. The converter should be bidirectional to charge and discharge the SCs.

Any converter that works in a bidirectional mode requires that the circuit work in a step-up mode in at least one direction. Unfortunately, the series resonant converter (SRC) is a step-down converter and uses a transformer to increase the voltage [5]. However, when the transformer works in the opposite direction, both the transformer and the SRC reduce the voltage so the final voltage is below the required value.

This can be better explained by Fig. 1. The voltage conversion ratio (M) for any type of bidirectional dc/dc converter, according to the ports shown in Fig. 1, is defined as $M_{21} = V_{2\mathrm{DC}}/V_{1\mathrm{DC}} (M_{12} = V_{1\mathrm{DC}}/V_{2\mathrm{DC}})$ when the power flow is from (to) $V_{1\mathrm{DC}}$ to (from) $V_{2\mathrm{DC}}$. In order to increase the output voltage and provide galvanic isolation, many converters include a transformer, and thus M_{12} and M_{21} depend on the transformer turns ratio (n). In these cases, a normalized voltage conversion gain can be defined as $m_{21} = V_{2\mathrm{DC}}/(n \cdot V_{1\mathrm{DC}})$ and $m_{12} = n \cdot V_{1\mathrm{DC}}/V_{2\mathrm{DC}}$, where the influence of the transformer turns ratio is excluded. Hence, the voltage conversion gain of a system including a transformer is expressed as $M_{21} = m_{21} \cdot n$ and $M_{12} = m_{12}/n$.

In an SRC, both m_{12} and m_{21} are less than one. Therefore, in order to increase the output voltage, a transformer is needed so that M_{21} can be greater than one. In this paper, a novel control method is developed. It consists of changing the switching pattern of the rectifier side of the SRC converter, so energy accumulation in the LC branch is achievable and an m greater than one is possible. This novel technique allows the SRC to be attached to several energy storage devices, such as batteries and SCs [6], [7].

In general, an energy storage device has a minimum and a maximum working voltage, and it is commonly attached to a constant dc line through a dc/dc converter [8]–[10]. In Fig. 1, $V_{1\mathrm{DC}}$ is attached to the energy storage device and $V_{2\mathrm{DC}}$ is attached to the constant voltage dc line. Considering the minimum and maximum voltage values of the energy storage device, the m_{21} values that make $V_{2\mathrm{DC}}$ constant are expressed in (1a) and (1b). In the opposite direction, the boundary values of m_{21} are expressed in (1c) and (1d) with $V_{2\mathrm{DC}}$ constant

$$V_{2\mathrm{DC}} = m_{21\mathrm{MAX}} \cdot n \cdot V_{1\mathrm{DC\,min}} \tag{1a}$$

$$V_{2\mathrm{DC}} = m_{21\,\mathrm{min}} \cdot n \cdot V_{1\mathrm{DCMAX}} \tag{1b}$$

$$V_{1\mathrm{DC\,min}} = m_{12\,\mathrm{min}} \cdot V_{2\mathrm{DC}}/n \tag{1c}$$

$$V_{1\mathrm{DCMAX}} = m_{12\mathrm{MAX}} \cdot V_{2\mathrm{DC}}/n. \tag{1d}$$

It can be seen that when $V_{1\mathrm{DC}}$ has the minimum voltage, m_{21} should be the maximum (1a) and m_{12} the minimum (1c). By multiplying (1a) with (1c) and (1b) with (1d), a pair of relations is obtained in (2)[Comp: Please link all the equations in the text throughout the article.]. These equations show the necessity of having an m (in any direction) greater than one. Assuming that the converter in Fig. 1 is a common SRC (where $m \leq 1$) and the ideal case, where $m_{12\mathrm{MAX}}$ and $m_{21\mathrm{MAX}}$ are equal to one, then the minimum values $(m_{12\mathrm{min}}$ and $m_{21\mathrm{min}})$ should also be one in order to satisfy (2). That means that the common SRC does not allow a voltage variation at one port when the other must be at fixed voltage. Therefore, a step-up mode is mandatory for dc/dc converters in that kind of application

$$1 = m_{12\mathrm{MAX}} \cdot m_{21\,\mathrm{min}} \tag{2a}$$

$$1 = m_{21\mathrm{MAX}} \cdot m_{12\,\mathrm{min}}. \tag{2b}$$

II. DC Analysis

The power stage schematic circuit of the SRC is presented in Fig. 2(a). Switches M1 to M8 are controlled by a 50% square wave oscillator that works above the resonant frequency (f_0). The system transfers energy from $V_{1\mathrm{DC}}$ to $V_{2\mathrm{DC}}$ based on that oscillator, whose frequency is called f_S (switching frequency). The gates of M1, 2, 3, 4, 7, and 8 (M5 and M6 remain off) are triggered as shown in Fig. 2(b). In the opposite power flow direction, the gates of M2, 4, 5, 8, and M6, 7 act like those of M1, 4, 7, 8 and M2, 3, respectively. A simplified circuit is shown in Fig. 2(c), which will be used to develop the dc model and the dc characteristics of the converter. V_1 and V_2 from Fig. 2(c) represent voltage sources that remain constant in a time interval. As shown in Fig. 2(c), the analysis does not consider the transformer turns ratio of the real converter, so the analysis is completely symmetric and it can be used in both directions. The addition of the transformer increases the voltage conversion ratio of the whole converter in one direction and decreases it in the same proportion in the opposite direction. This analysis considers that $n \cdot V_{1\mathrm{DC}}$ is $V_{\mathrm{IN}}, V_{2\mathrm{DC}}$ is V_{OUT}, and R is the load resistor.

The circuit has three time intervals $(t_1, t_2$, and $t_3)$ due to the commutation of switches M1 to M8, so the three possible values for the (V_1, V_2) pair are listed in (3). The time intervals are related as shown in (3). F is the normalized frequency, f_S/f_0

$$(V_1, V_2) = \begin{cases} V_{\mathrm{IN}}, 0 \\ -V_{\mathrm{IN}}, V_{\mathrm{OUT}} \quad V_T = V_1 - V_2 \\ -V_{\mathrm{IN}}, -V_{\mathrm{OUT}} \end{cases} \tag{3}$$

$$t_1 = t_2 + t_3 = \frac{\pi}{\omega_S} = \frac{\pi}{\omega_0 \cdot F}.$$

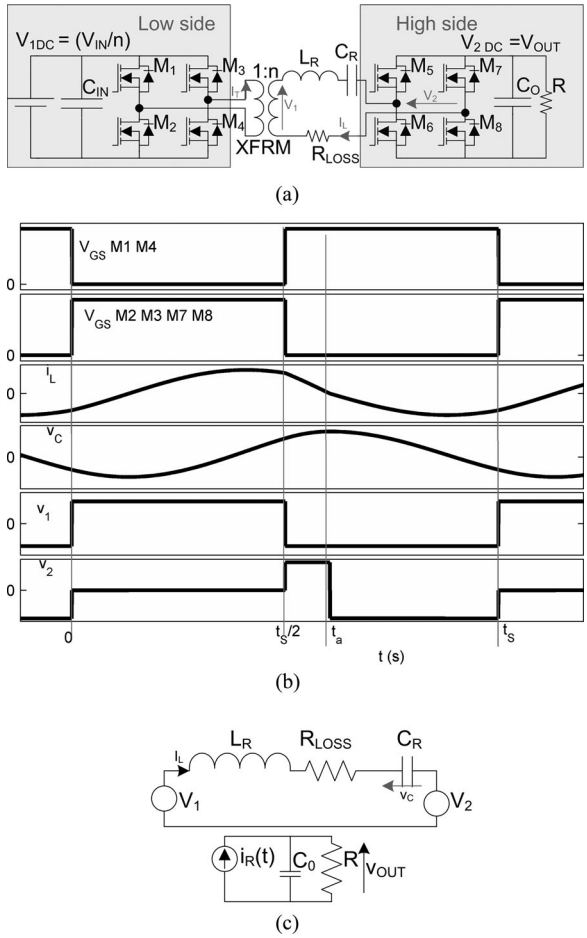

Fig. 2. DC/DC converter: (a) schematic, (b) waveforms, and (c) simplified circuit.

The *LC* branch is governed by the following equation:

$$V_T = L_R \cdot C_R \cdot \frac{d^2 v_C}{dt^2} + R_{\mathrm{LOSS}}.C_R \frac{dv_C}{dt} + v_C$$
$$i_L = C_R \frac{dv_C}{dt}. \tag{4}$$

The solution is

$$v_{C(n)} = v_{C1(n)} \cdot \cos(\omega_0 \cdot t + \varphi_n) \cdot e^{-kt} + V_{T(n)}$$
$$i_{L(n)} \approx -\frac{v_{C1(n)}}{Z_0} \cdot \sin(\omega_0 \cdot t + \varphi_n) \cdot e^{-kt} \tag{5}$$

where $v_{C(n)}, v_{C1(n)}, \varphi_n$ are the capacitor voltage, the capacitor initial voltage, and the initial phase for the nth interval. The attenuator factor is $k = R_{\mathrm{LOSS}}/(2L_R)$ and the characteristic impedance $Z_0 = (L_R/C_R)^{1/2}$. Equation (5) can be normalized based on the state-plane method [11], [12]. This method is commonly used in the analysis of continuous and discontinuous series and parallel resonant converters, which is why it is used in this paper to show the state-plane of the bidirectional SRC in a step-up mode. The solution based on the normalization is

$$m_{C(n)}(t) = H_{(n)} \cdot \cos(\omega_0 \cdot t + \varphi_n) \cdot e^{-kt} + m_{T(n)}$$
$$j_{L(n)} \approx -H_{(n)} \cdot \sin(\omega_0 \cdot t + \varphi_n) \cdot e^{-kt}. \tag{6}$$

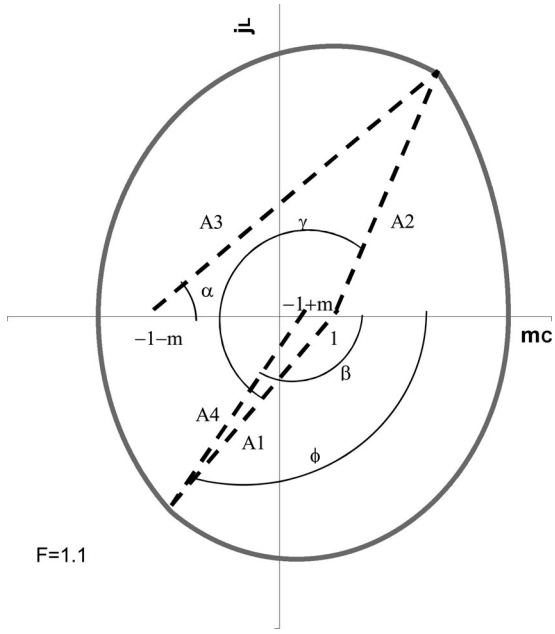

Fig. 3. State-plane representation of the step-up SRC ($R_{\mathrm{LOSS}} = 0$).

The method normalizes the capacitor voltage with the input voltage $V_{1\mathrm{DC}}$, and the inductor current with the input voltage and the characteristic impedance $Z_0 = (L_R/C_R)^{1/2}$. Consequently the normalized capacitor voltage is $m_C = v_C/V_{\mathrm{IN}}$, the normalized inductor current is $j_L = i_L \cdot Z_0/V_{\mathrm{IN}}$, and the conversion voltage ratio of each time interval is $m_{T(n)} = V_{T(n)}/V_{1\mathrm{N}}$. Therefore, in the m_C–j_L plane, the solution represents an arc of radius $H_{(n)}$ (for $R_{\mathrm{LOSS}} = 0$) with the center in $(m_C, j_L) = (0, m_{T(n)})$. The subindex n refers to the time interval from 1 to 3. Thus, three arcs form a closed curve in the plane as shown in Fig. 3. A lossless example is shown in order to clarify the concepts. If power losses are considered, the arcs have an initial radius and a smaller final radius. Each arc starts when the previous one finishes due to the capacitor voltage and inductor current continuity constrain. This is the key to obtaining the voltage conversion ratio, M. This analysis does not consider any transformer ratio, so $m = M$. The whole curve in Fig. 3 was obtained by simulating the circuit in Fig. 2(a) in PSIM, and it shows the particular case when $F = 1.1$. In addition, the values of A_1 to A_3 are shown. The arc with A_1 radius represents the half of the switching period, $t_S/2.\gamma, \alpha, \beta$ are the arc angles of the first, second, and third interval, respectively, and ϕ represents the initial angle.

In the common analysis the state plane provides enough information to obtain a closed-form expression for the voltage conversion ratio as a function of R and f_S. Unfortunately, for this converter the solution could not be obtained analytically, so it was obtained numerically. The equations that should be solved to obtain m, including the losses, are presented in (8). The first five equations in (8) are the initial conditions for the three time-intervals mentioned earlier. The sixth equation is the relation between the angle (γ) of the accumulation time-interval (the first half of the switching period) and the resonant frequency.

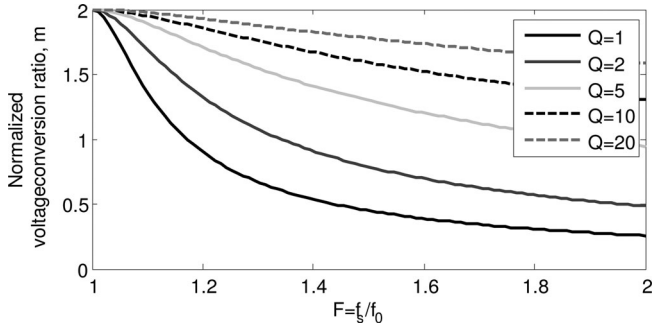

Fig. 4. Normalized voltage conversion ratio, m versus f_s/f_0 for different quality factors (Q).

Each angle is defined as

$$\gamma = \omega_0 \cdot t_1 \tag{7a}$$

$$\omega_0 = 2 \cdot \pi \cdot f_0 \tag{7b}$$

$$\alpha = \omega_0 \cdot t_2 \tag{7c}$$

$$\beta = \omega_0 \cdot t_3. \tag{7d}$$

The other time-intervals (energy transfer intervals) form the second half of the switching period, as the sixth equation in (8) expresses. The last equation relates the converter output voltage with the state-plane. That equation is based on the electric charge of C_R. The maximum difference in C_R voltage (which in the state-plane is m_{CMAX}–$m_{C\,\min}$) is proportional to the charge transferred to the load. This charge is $I_{\rm OUT}.T_{\rm S}$. Normalizing this, $m_{CMAX} - m_{C\,\min} = 2 \cdot \gamma \cdot m/r$ where r is the normalized load resistor (R/Z_0). The first member of the seventh equation in (8) is obtained from Fig. 3, but includes the power losses

$$H_1 \cdot \exp(\frac{-k\gamma}{\omega_0}) \cdot \cos(\phi + \gamma) + 1 = H_2 \cdot \cos(\alpha) - 1 - m$$

$$H_2 \cdot \exp(\frac{-k\alpha}{\omega_0}) - 1 - m = H_3 - 1 + m$$

$$H_3 \cdot \exp(\frac{-k\beta}{\omega_0}) \cdot \cos(\beta) - 1 + m = H_1 \cdot \cos(\phi) + 1$$

$$H_1 \cdot \exp(\frac{-k\gamma}{\omega_0}) \cdot \sin(\phi + \gamma) = H_2 \cdot \cos(\alpha)$$

$$H_3 \cdot \exp(\frac{-k\beta}{\omega_0}) \cdot \sin(\beta) = H_1 \cdot \sin(\phi)$$

$$\frac{f_S}{f_0} = \frac{\gamma}{\pi} = \frac{\alpha + \beta}{\pi}$$

$$H_1 \cdot \exp\left[\frac{-k(\pi - \phi)}{\omega_0}\right] + H_3 - 2 + m = \frac{m \cdot 2 \cdot \gamma}{r}. \tag{8}$$

Using (8), Fig. 4 shows m as a function of F for different values of the load resistor (Q factor is defined as $Q = 1/r = Z_0/R$ for a lossless circuit). The influence of considering a loss resistance is shown in Fig. 5 for the particular case in which $R = Z_0$. It can be observed that the maximum value of m is reduced as $R_{\rm LOSS}$ increases (ideally $m = 2$ for lossless case).

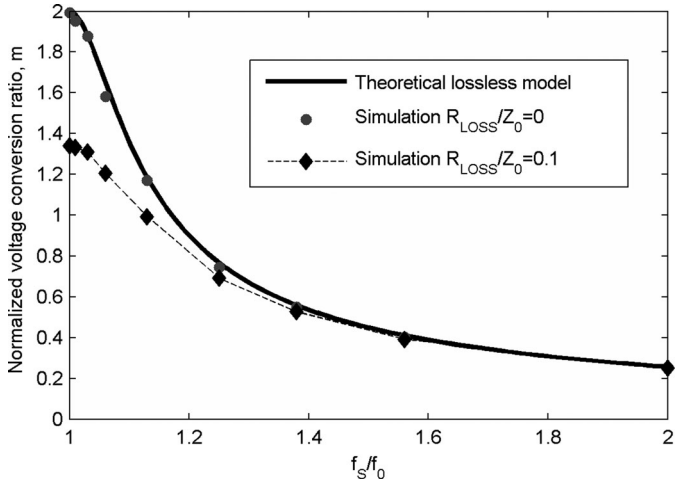

Fig. 5. Normalized voltage conversion ratio, m versus f_s/f_0 including $R_{\rm LOSS}$ for $R = Z_0$.

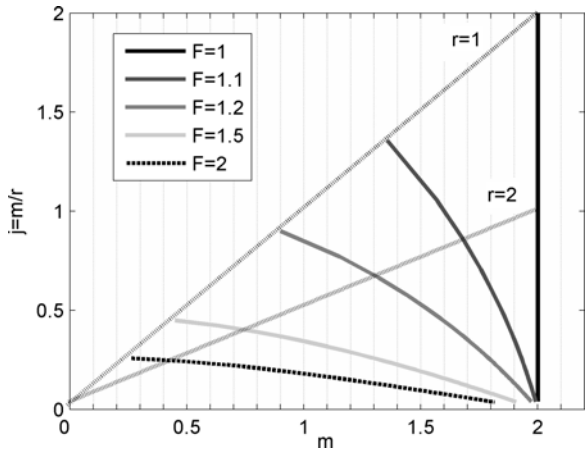

Fig. 6. Output characteristics of a step-up SRC.

This converter—similar to other converters such as the dual active bridge (DAB) [13]–[16], single active bridge [17], and many resonant converters [18]–[22]—has an m which depends on both the load and the switching frequency. Fig. 6 shows the output characteristics of the converter by considering the lossless case. In the figure, two load lines are plotted; this plot is useful because if the load and the m ranges are defined, the frequency variation is known. As an example, if the normalized load variation is from 1 to 2, and m is from 0.8 to 1.35, the frequency variation is from $f_S = f_0$ to $f_S = 1.5 f_0$. Fig. 7 shows α and β as function of F for $r = 1$.

III. AC Analysis

The dc analysis is useful for selecting components and determining the switching frequency range. However, a small-signal control transfer function is needed in order to design the controller of the converter. Thus, a proper control that modifies the switching frequency to keep the output voltage constant can be designed. There are several methods for analyzing the small-signal variation of resonant dc/dc converters [23]–[27]. In this paper, the averaged state-space method is used. First, the

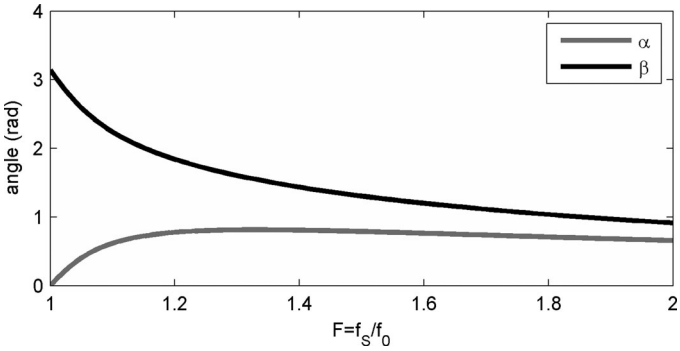

Fig. 7. Angle of the transfer arcs (α and β) versus $F, r = 1$.

state-space model is solved for each time interval. Then continuity constrains in i_L and v_C are applied in the boundary conditions to join the solutions corresponding to each time interval. The analysis is based on the circuit in Fig. 2(c), where i_R is defined as the rectified current, meaning that i_R is zero for the accumulation time interval and it is $|i_L|$ for the transfer intervals (second and third interval). Thus, steady-state equations for the state and output variables are first obtained, and then small-signal perturbations are applied to those equations in order to obtain the ac small-signal characteristics of the system. In this paper, only the control-to-output transfer function is presented, but any other transfer function can be calculated by this method. A detailed exampled is given in [28].

The state-space models for the three time-intervals are shown in (9). The state vector is $x(t) = [i_R \quad v_C \quad v_{\rm OUT}]^T$ for any time interval

$$\frac{d\mathbf{x}}{dt} = \mathbf{A_n} \cdot \mathbf{x} + \mathbf{b_n} \cdot v_{\rm IN}, v_{\rm OUT} = \mathbf{c} \cdot \mathrm{x},$$

where n can be 1, 2, 3 and

$$\mathbf{A_1} = \begin{bmatrix} -\frac{R_{\rm LOSS}}{L_R} & \frac{-1}{L_R} & 0 \\ 1/C_R & 0 & 0 \\ 0 & 0 & \frac{1}{RC_0} \end{bmatrix}, \quad \mathbf{b_1} = \begin{bmatrix} \frac{1}{L_R} \\ 0 \\ 0 \end{bmatrix}$$

$$\mathbf{A_2} = \begin{bmatrix} -\frac{R_{\rm LOSS}}{L_R} & \frac{-1}{L_R} & \frac{-1}{L_R} \\ 1/C_R & 0 & 0 \\ \frac{1}{C_0} & 0 & \frac{1}{RC_0} \end{bmatrix}, \quad \mathbf{b_3} = \mathbf{b_2} = -\mathbf{b_1}$$

$$\mathbf{A_3} = \begin{bmatrix} -\frac{R_{\rm LOSS}}{L_R} & \frac{-1}{L_R} & \frac{1}{L_R} \\ 1/C_R & 0 & 0 \\ \frac{-1}{C_0} & 0 & \frac{1}{RC_0} \end{bmatrix}, \quad \mathbf{c} = [\,0 \quad 0 \quad 1\,]. \tag{9}$$

The solution is

$$\mathbf{x}(t) = e^{\mathbf{A_1} \cdot t} \cdot \mathbf{x}(0) + \mathbf{A_1^{-1}} \cdot e^{\mathbf{A_1} \cdot t} \cdot \mathbf{b_1} \cdot V_{\rm IN} 0 \le t \le \frac{T_S}{2}$$

$$\mathbf{x}(t) = e^{\mathbf{A_2} \cdot t} \cdot \mathbf{x}\left(\frac{t_S}{2}\right) + \mathbf{A_2^{-1}} \cdot e^{\mathbf{A_2} \cdot t} \cdot \mathbf{b_2} \cdot V_{\rm IN} \frac{T_S}{2} \le t \le t_a$$

$$\mathbf{x}(t) = e^{\mathbf{A_3} \cdot t} \cdot \mathbf{x}(t_a) + \mathbf{A_3^{-1}} \cdot e^{\mathbf{A_3} \cdot t} \cdot \mathbf{b_3} \cdot V_{\rm IN} t_a \le t \le T_S. \tag{10}$$

The steady-state condition means that $\mathbf{x}(0) = \mathbf{x}(T_S)$. Thus, by using (9), t_a can be obtained, which is directly related with α in the dc analysis. In addition, $v_{\rm OUT}$ can be obtained: $v_{\rm OUT}(t) = \mathbf{c} \cdot \mathbf{x}(t)$. The averaged method calculates the two basic equations that should be perturbed to perform the ac analysis

$$T_S \cdot V_{\rm OUT} = \int_0^{t_S} v_{\rm OUT}(t) \cdot dt = \mathbf{k_1} \cdot \mathbf{x}(0) + k_2 \cdot V_{\rm IN} \tag{11a}$$

$$\mathbf{x}(T_S) = \mathbf{A} \cdot \mathbf{x}(0) + \mathbf{B} \cdot V_{\rm IN}. \tag{11b}$$

Equation (11a) is the average of the output value and (11b) is extracted from (10) in order to represent $x(T_S)$ as an explicit function of $x(0)$ and $V_{\rm IN}$. k_1 and k_2 can be obtained by solving (11a). The variables that depend on f_S should be perturbed, e.g., $T_S = \overline{T}_S + \hat{t}_S, t_a = \overline{T}_a + \hat{t}_a, \mathbf{x}(0) = \overline{\mathbf{X}}(0) + \hat{\mathbf{x}}(0)$, etc., with $\hat{t}_S = -1 \Big/ \overline{F}_S^2 \cdot \hat{f}_S$, etc. The variable with a line in the top indicates averaged values in one period, T_S, while the hatted variables indicate a small perturbation. Thus, two perturbed equations are obtained from (11)

$$(\overline{V}_{\rm OUT} + \hat{v}_{\rm OUT}) \cdot (\overline{T}_S + \hat{t}_S) = (\overline{\mathbf{k}}_\mathbf{1} + \hat{\mathbf{k}}_\mathbf{1}) \cdot [\overline{\mathbf{X}}(0) + \hat{\mathbf{x}}(0)] + (\overline{k}_2 + \hat{k}_2) \cdot V_{\rm IN} \tag{12a}$$

$$\hat{\mathbf{x}}(T_S) + \overline{\mathbf{X}}(T_S) = [\overline{\mathbf{A}} + \hat{\mathbf{A}}] \cdot [\overline{\mathbf{X}}(0) + \hat{\mathbf{x}}(0)] + [\overline{\mathbf{B}} + \hat{\mathbf{B}}] \cdot V_{\rm IN}. \tag{12b}$$

The control-to-output transfer function is obtained from (12a) by expressing the equation as an explicit function of $\hat{f}_S$ and $\hat{\mathbf{x}}(0)$ and by replacing them with their Laplace transforms [$f_S(s)$ and $\mathbf{x}(s)$]. Equation (12b) is used to express $x(s)$ as a function of $f_S(s)$. The final equations are

$$v_{\rm OUT}(s) = \mathbf{h^T} \cdot \mathbf{x}(s) + k_S \cdot f_S(s) \tag{13a}$$

$$\mathbf{x}(s) = [\mathbf{I}e^{sT_S} - \mathbf{A}]^{-1} \cdot \mathbf{d_S} \cdot f_S(s) \tag{13b}$$

where h, k_S and d_S are obtained from (12) and depend on $R_{\rm LOSS}, L_R, C_R, R, V_{\rm IN}$, and C_0. Thus, the control-to-output transfer function is obtained from (13). A computer program was developed in MATLAB to compare the theoretical model with results from simulations and experimental measurements.

IV. Experimental Results

In order to validate the theoretical analysis presented in Sections IV and V, the voltage conversion ratio and the control-to-output transfer function were measured in a prototype shown in Fig. 8. This prototype can deliver up to 6 kW between two ports: the low side port accepts voltages from 60 to 120 V and the high side port has a fixed voltage of 360 V. The resonant frequency is 40 kHz. L_R, C_R, and C_0 are 72 μH, 220 nF, and 160 μF, respectively. Two load resistors are tested: $R_1 = 20\ W$ and $R_2 = 140\ W$. Fig. 9 shows the comparison of the voltage conversion ratio between the theoretical model, the data

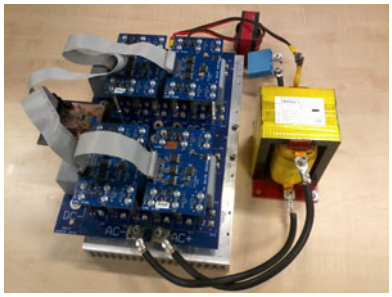

Fig. 8. Prototype.

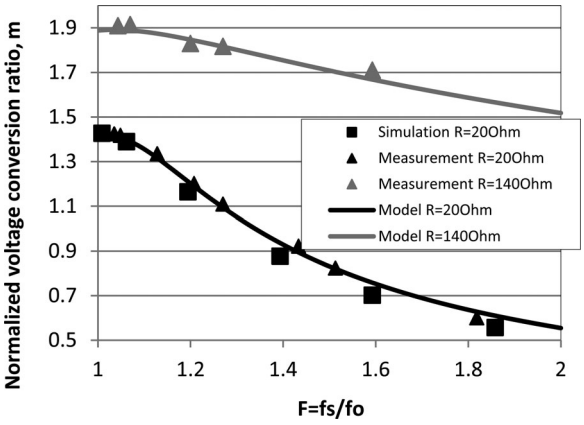

Fig. 9. DC characteristics.

extracted from simulations in PSIM, and the measurements for the two loads. It can be noted that the results obtained from the theoretical model are in good agreement with the experimental and the simulated data. The waveforms for M1 and M7 are shown in Fig. 10 for both R_1 and R_2 resistors. It can be seen that the turn-on process occurs at zero voltage for M1 (and also M2, 3, and 4 because the waveforms are the same). This zero-voltage turn-on is due to the converter working above its resonance frequency. The turn-off process is still a hard switching, but for heavy loads (low R value) the converter works near its resonance so the I_D current at the moment of turn-off is reduced compared to a phase-shift DAB [29]. The waveforms for M7 show that a zero-voltage it also achieves a turn-on transition and a hard switching turn-off process. M4 and M5 work as diodes, and M8 has hard-switching turn-on and a zero-voltage turn-off (its drain current is the opposite of M7 during the on-time). In addition, as the converter always works above the resonance frequency, the impedance that the input bridge (M1 to M4 for the low-to-high voltage power flow) "sees" is inductive impedance, so the current lags the voltage. Thus, the turn-on process is a zero-voltage transition even in transient conditions.

Fig. 11 shows the ac behavior of the system. The absolute value of the control-to-output transfer function was measured, simulated, and modeled for the two loads at different frequencies. It can be observed that there is good agreement for low frequencies and a tolerable deviation for higher frequencies. The deviation is small enough to design the controller.

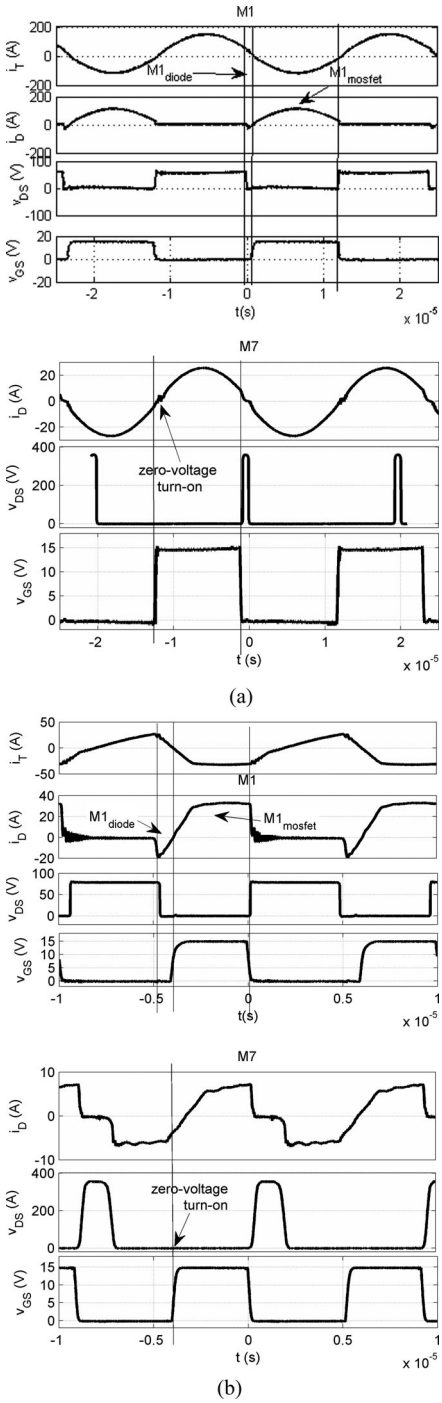

Fig. 10. M1 and M7 switching waveforms for (a) full-load and (b) light load condition.

The design procedure begins with the plot of the output characteristics for the lightest and the heaviest load resistors and for the two limits of M: 0.75 and 1.5 (step-up). Fig. 12 shows this plot, which can be used to determine the normalized frequency switching range (F): in this case from 1.05 to 3.9 (loads from 20 to 140 Ω). Then, based on the proposed ac model, the control-to-output transfer function is plotted in Fig. 13 for the following four cases: maximum/minimum load and maximum/minimum input voltage. These transfer functions include

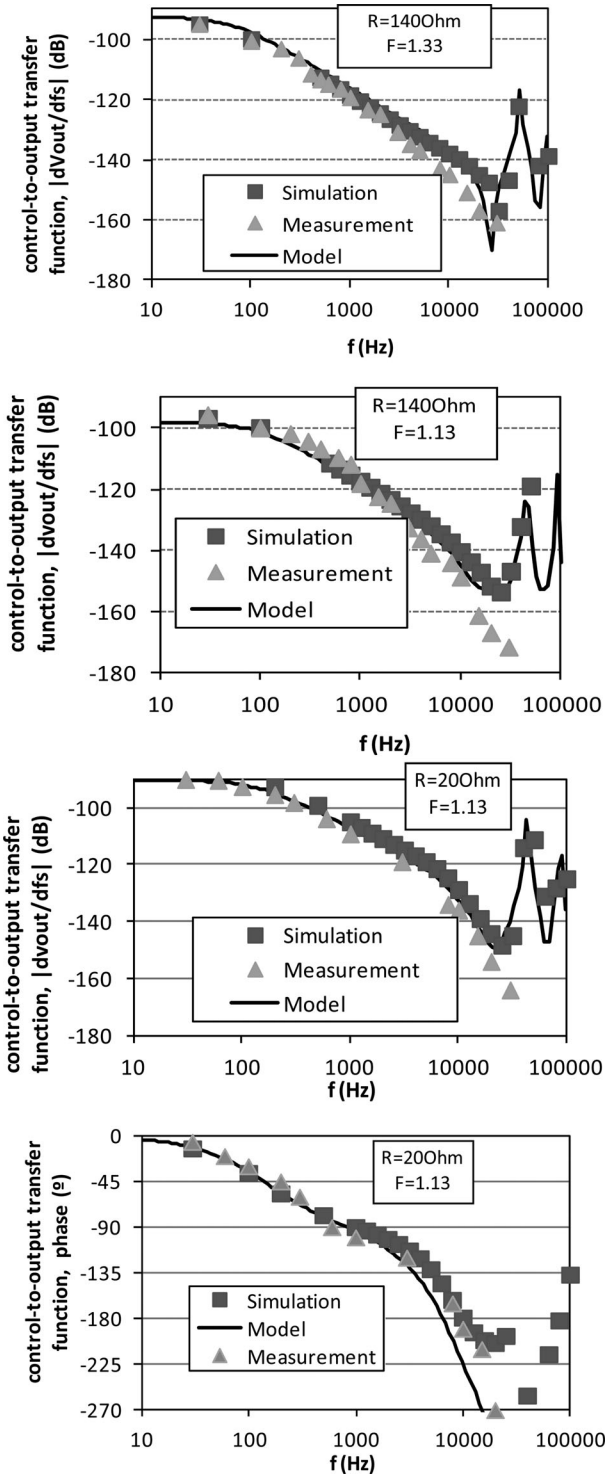

Fig. 11. Control-to-output transfer function for several static points.

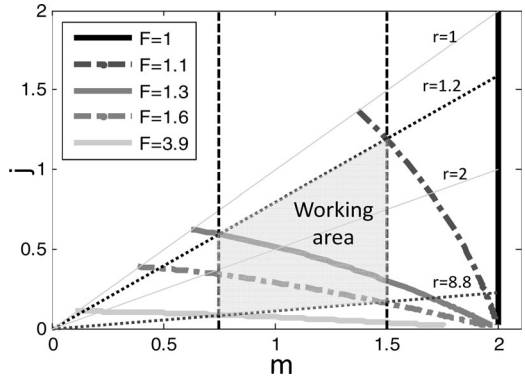

Fig. 12. Prototype output characteristics of a step-up SRC.

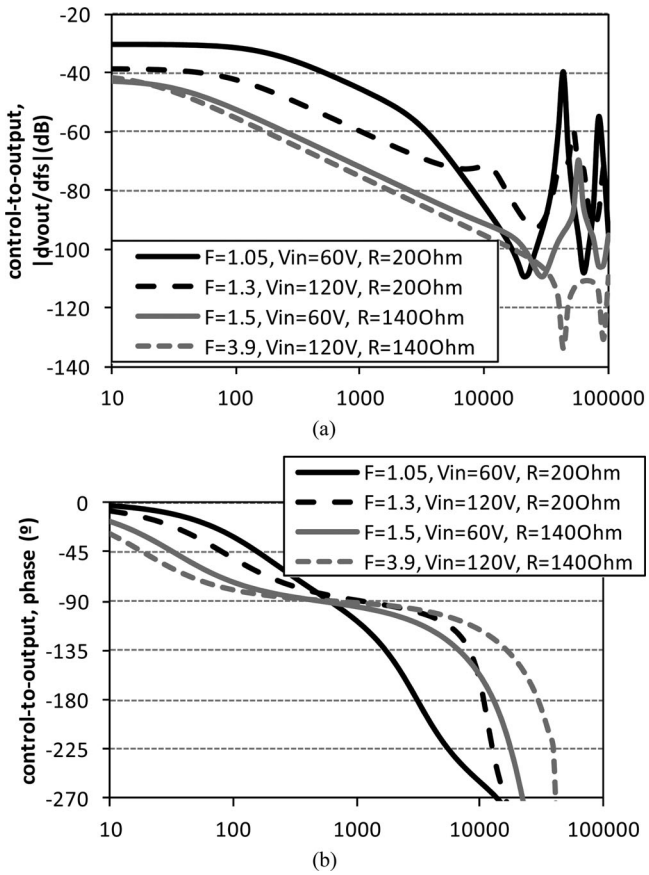

Fig. 13. Control-to-output transfer function modeled for the prototype: (a) magnitude and (b) phase.

the variation in V_{IN}, and thus their values become similar at low frequencies.

The proposed controller is a PI controller. Fig. 13 aids in the parameter selection. It suggests that the cut-off frequency for the heaviest load (20 Ω) and $V_{\rm IN} = 60\,V$ should be 1.7 kHz. Therefore, the gain of the control chain should be approximately +50 dB V/Hz. The control diagram is presented in Fig. 14. The control chain gain at 1.7 kHz $(K_f * K_P * K_{\rm ATT})$ is +50 dB. The attenuator factor, $K_{\rm ATT}$, is −40 dB, and the VCO factor is $K_f = 78\,{\rm dB\,Hz}/V$, so K_P should be around 4. The integral time constant is set to 0.32 ms (around 500 Hz). In order to verify the closed-loop behavior, a load-step response between 20 and 40 Ω is presented in Fig. 15. The time response of the converter is 4 and 8 ms for the heavy-load connection and disconnection, respectively. The input current overshoot is lower than 5%.

An efficiency comparison between the present converter and a DAB converter using phase-shift control is presented in Fig. 16. Our design was aided by dos Santos *et al.* [29]. It can be seen

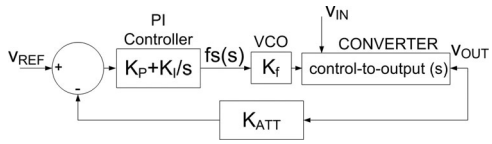

Fig. 14. Control diagram.

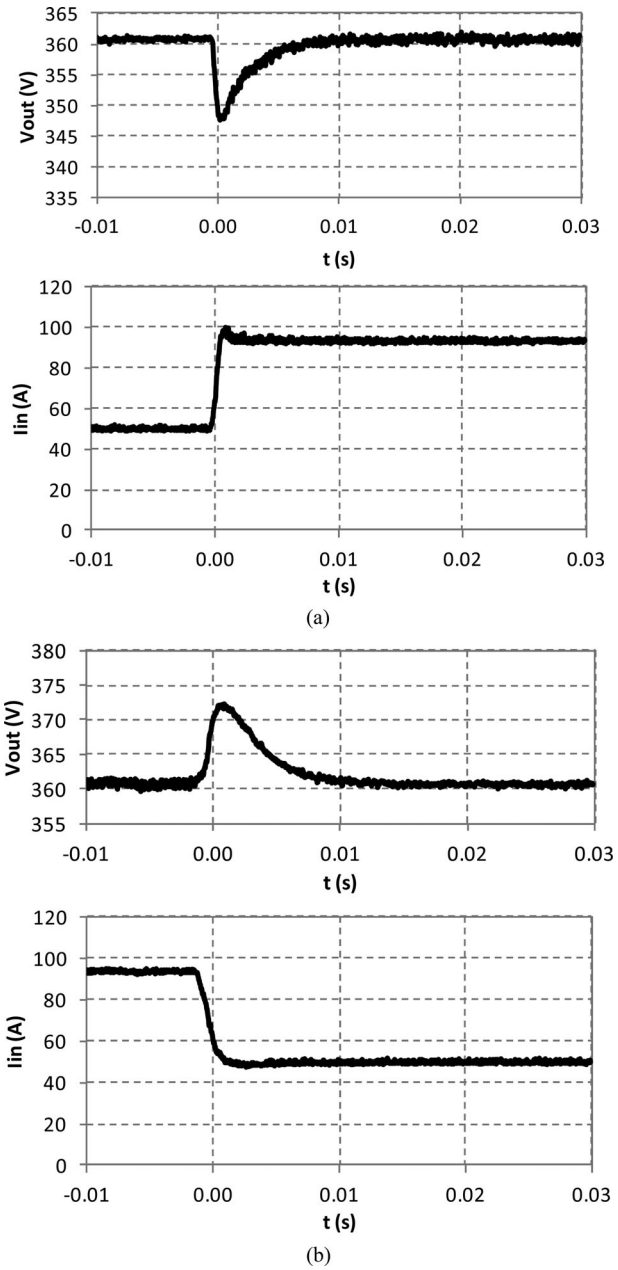

Fig. 15. Load-step response load-step response (a) from 40 to 20 Ω, andxbrk (b) from 20 to 40 Ω.

that the DAB converter is very efficiency at high power, but as the output power decreases so does its efficiency. Simulations were carried out using the same model for the MOSFETs in both DAB and SRC converters. However, in the case of the DAB converter, a value of $R_{\mathrm{LOSS}}/2$ was used instead of the value

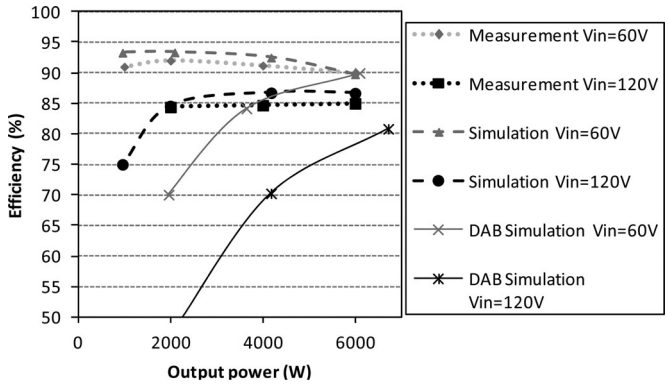

Fig. 16. Efficiency.

R_{LOSS}, which was used for the SRC. This is because the DAB converter does not have the series capacitor C_R, so there is one fewer component in series in the R_{LOSS} branch.

R_{LOSS} was adjusted by taking into account the efficiency of the converter in the lowest input voltage condition (60 V). Fig. 16 shows that the efficiency of the SRC is flatter and does not decrease as much as the efficiency that corresponds to the DAB converter when the power transfer is reduced. This is mainly attributed to the shape of the current in the R_{LOSS} branch, and it represents the main advantage of the SRC over the DAB converter controlled by phase-shift modulation. For heavy loads, both converters have similar efficiency. The SRC has lower switching losses because the switching turn-off transitions occur closer to zero-current (f_S close to f_0) than in the DAB. However, the conduction losses for the SRC are higher than for the DAB because of the sinusoidal waveforms with a higher current peak. Therefore, the efficiency is quite similar.

On the other hand, for light loads, the DAB keeps high currents circulating through its inductor although the output current is not high, while the SRC increases its impedance by increasing the switching frequency. Thus, the conduction losses go down. This is the reason for having better behavior at light loads. The switching losses remain because the switching current decreases but the switching frequency increases. The main disadvantage of the presented SRC is that the switching frequency is not constant, so the components should behave well for the whole frequency range.

As the circuit is completely symmetric, the efficiency plot is only presented in one direction. In the other power flow direction, the circuit uses M5 to M8 as M1 to M4 in the low-to-high voltage power flow direction. M5, M8, M2, and M4 are triggered as M2, M3, M7, and M8 in Fig. 2(b), and M6 and M7 are triggered as M1 and M4. The waveforms in Fig. 10 are similar, but M1 is exchanged for M6 and M7 for M4.

V. Conclusion

This paper shows a comprehensive analysis of both the dc and small-signal ac behaviors of a new technique that makes it possible to use the classical SRC as a step-up converter. This is particularly useful for bidirectional power flow applications where one port is attached to an energy accumulator device, such

as a battery or SC bank, and the other port is attached to a fixed dc line. The paper presents a prototype of a bidirectional dc/dc converter that can transfer power up to 6 kW. The experimental measurements validate the dc and ac analysis. Furthermore, a design procedure for a simple controller is shown and applied to the prototype. A load-step process is performed to validate the controller.

Finally, the converter efficiency is plotted for several-transfer power values and compared to the simulated results of a DAB converter controlled by a phase-shift modulation. It shows that the SRC presents similar efficiency for high power transfer and it presents greater efficiency for light loads, which represents the main advantage of this converter.

ACKNOWLEDGMENT

The authors would like to thank Wendy Baldwin, Fernando Martín, Ignacio Sanchez-Guardamino, and Jose Antonio Aguirre for their invaluable help.

REFERENCES

[1] R. Kotz and M. Carlen, "Principles and applications of electrochemical capacitors," *Electrochimica Acta*, vol. 15, no. 15/16, pp. 2483–2498, Dec. 1999.

[2] R. A. Dougal, S. Liu, and R. E. White, "Power and life extension of battery—Ultracapacitor," *IEEE Trans. Compon. Packag. Technol.*, vol. 25, no. 1, pp. 120–131, Mar. 2002.

[3] F. Ongaro, S. Saggini, and P. Mattavelli, "Li-ion battery-supercapacitor hybrid storage system for a long lifetime, photovoltaic-based wireless sensor network," *IEEE Trans. Power Electron.*, vol. 27, no. 9, pp. 3944–3952, Sep. 2012.

[4] M.-E. Choi, S.-W. Kim, and S.-W. Seo, "Energy management optimization in a battery/supercapacitor hybrid energy storage system," *IEEE Trans. Smart Grid*, vol. 3, no. 1, pp. 463–472, Mar. 2012.

[5] M. K. Kazimierczuk, "Resonant power converters," 1995.

[6] A. Chu and P. Braatz, "Comparison of commercial supercapacitors and high-power lithium-ion batteries for power-assist applications in hybrid electric vehicles I. Initial characterization," *J. Power Sources*, vol. 102, no. 1, pp. 236–246, 2002.

[7] S. Moayedi, F. Cingoz, and A. Davoudi, "Accelerated simulation of high-fidelity models of supercapacitors using waveform relaxation techniques," *IEEE Trans. Power Electron.*, vol. 28, no. 11, pp. 4903–4909, Nov. 2013.

[8] J. Cao and A. Emadi, "A new battery/ultracapacitor hybrid energy storage system for electric, hybrid, and plug-in hybrid electric vehicles," *IEEE Trans. Power Electron.*, vol. 27, no. 1, pp. 122–132, Jan. 2012.

[9] A. Lahyani, P. Venet, A. Guermazi, and A. Troudi, "Battery/supercapacitors combination in uninterruptible power supply (UPS)," *IEEE Trans. Power Electron.*, vol. 28, no. 4, pp. 1509–1522, Apr. 2013.

[10] F. Nejabatkhah, S. Danyali, S. Hosseini, M. Sabahi, and S. Niapour, "Modeling and control of a new three-input DC–DC boost converter for hybrid PV/FC/battery power system," *IEEE Trans. Power Electron.*, vol. 27, no. 5, pp. 2309–2324, May 2012.

[11] C. Q. Lee and K. Siri, "Analysis and design of series resonant converter by state-plane diagram," *IEEE Trans. Aerosp. Electron. Syst.*, vol. AES-22, no. 6, pp. 757–763, Nov. 1986.

[12] K. Siri, I. Batarseh, and C. Q. Lee, "Frequency response for the conventional parallel resonant converter based on the state-plane diagram," *IEEE Trans. Circuits Syst. I: Fundam. Theory Appl.*, vol. 40, no. 1, pp. 33–42, Jan. 1993.

[13] M. N. Kheraluwala, R. W. Gascoigne, D. M. Divan, and E. D. Baumann, "Performance characterization of a high-power dual active bridge DC-to-DC converter," *IEEE Trans. Ind. Appl.*, vol. 28, no. 6, pp. 1294–1301, Nov./Dec. 1992.

[14] A. K. Jain and R. Ayyanar, "PWM control of dual active bridge: Comprehensive analysis and experimental verification," *IEEE Trans. Power Electron.*, vol. 26, no. 4, pp. 1215–1227, Apr. 2011.

[15] H. Qin and J. W. Kimball, "Generalized average modeling of dual active bridge DC–DC converter," *IEEE Trans. Power Electron.*, vol. 27, no. 4, pp. 2078–2084, Apr. 2012.

[16] B. Zhao, Q. Song, and W. Liu, "Power characterization of isolated bidirectional dual-active-bridge DC–DC converter with dual-phase-shift control," *IEEE Trans. Power Electron.*, vol. 27, no. 9, pp. 4172–4176, Sep. 2012.

[17] G. D. Demetriades and H. P. Nee, "Characterisation of the soft-switched single-active bridge topology employing a novel control scheme for high-power DC–DC applications," in *Proc. IEEE 36th Power Electron. Spec. Conf.*, Jun. 16, 2005, pp. 1947–1951.

[18] M. K. Kazmierczuk, D. Czarkowski, and N. Thirunarayan, "A new phase-controlled parallel resonant converter," *IEEE Trans. Ind. Electron.*, vol. 40, no. 6, pp. 542–552, Dec. 1993.

[19] C. L. Chia and E. K. K. Sng, "A novel robust control method for the series–parallel resonant converter," *IEEE Trans. Power Electron.*, vol. 24, no. 8, pp. 1896–1904, Aug. 2009.

[20] H. B. Kotte, R. Ambatipudi, and K. Bertilsson, "High-speed (MHz) series resonant converter (SRC) using multilayered coreless printed circuit board (PCB) step-down power transformer," *IEEE Trans. Power Electron.*, vol. 28, no. 3, pp. 1253–1264, Mar. 2013.

[21] R. Beiranvand, B. Rashidian, M.-R. Zolghadri, and S. M. H. Alavi, "A design procedure for optimizing the LLC resonant converter as a wide output range voltage source," *IEEE Trans. Power Electron.*, vol. 27, no. 8, pp. 3749–3763, Aug. 2012.

[22] J. Zhang, J. Wang, G. Zhang, and Z. Qian, "A hybrid driving scheme for full-bridge synchronous rectifier in LLC resonant converter," *IEEE Trans. Power Electron.*, vol. 27, no. 11, pp. 4549–4561, Nov. 2012.

[23] I. Batarseh and K. Siri, "Generalized approach to the small signal modelling of DC-to-DC resonant converters," *IEEE Trans. Aerosp. Electron. Syst.*, vol. 29, no. 3, pp. 894–909, Jul. 1993.

[24] S. R. Sanders, J. M. Noworolski, X. Z. Liu, and G. C. Verghese, "Generalized averaging method for power conversion circuits," *IEEE Trans. Power Electron.*, vol. 6, no. 2, pp. 251–259, Apr. 1991.

[25] T. Ninomiya, M. Nakahara, T. Higashi, and K. Harada, "A unified analysis of resonant converters," *IEEE Trans. Power Electron.*, vol. 6, no. 2, pp. 260–270, Apr. 1991.

[26] A. F. Witulski, A. F. Hernandez, and R. W. Erickson, "Small signal equivalent circuit modeling of resonant converters," *IEEE Trans. Power Electron.*, vol. 6, no. 1, pp. 11–27, Jan. 1991.

[27] V. Vorperian, "Approximate small-signal analysis of the series and the parallel resonant converters," *IEEE Trans. Power Electron.*, vol. 4, no. 1, pp. 15–24, Jan. 1989.

[28] V. Vorperian, "Analysis of resonant converters," Ph.D. dissertation, California Inst. of Technology, CA, USA, 1984.

[29] W. M. dos Santos, M. S. Ortmann, R. Schweitzer, S. A. Mussa, and D. C. Martins, "Design and conception of a DAB converter (dual active bridge) using the gyrators theory," in *Proc. Brazilian Power Electron. Conf.*, Sep. 11–15, 2011, pp. 359–364.

Federico Martin Ibanez was born in Buenos Aires, Argentina, in 1982. He received the B.S. degree in electronic engineering from the National Technological University (UTN), Buenos Aires, in 2008 and the Ph.D. degree in power electronics from the University of Navarra, San Sebastián, Spain.

Since 2006 to 2009, he was part of the Electronics Department, UTN. He is currently part of the Power Electronics Group of Centro de Estudios e Investigaciones Técnicas de Gipuzkoa. His research interests include the areas of high-power dc/dc converters for applications related to energy storage, supercapacitors and smartgrids.

Jose Martin Echeverria was born in San Sebastian, Spain, in 1972. He received the M.Sc. and Ph.D. degrees in electrical engineering from the University of Navarra, Spain, in 1996 and 2005, respectively.

He started to work as a Researcher at CEIT in 1997 and has been an Associate Professor at the University of Navarra since 2011. Currently he works in the Electronic and Communications Department at CEIT within the Industrial and Power systems group. He has been involved in international and national projects related to power electronics, energy storage technologies and the development of intelligent power electronics converters.

Javier Vadillo was born in Bilbao, Spain, in 1978. He received the B.S. degree in electronic engineering from the University of the Basque Country (UPV/EHU), Spain, in 2002, the B.S. degree in physics from the University of Cantabria, Spain, in 2003, and the Ph.D. degree in the electronics and communications program from the University of Navarra, Spain, in 2011.

Since 2004, he has been with the Electronics and Communications Department in CEIT-IK4, San Sebastian, Spain. He is also a Lecturer with TECNUN, University of Navarra. His research interests include the areas of electric energy storage systems (supercapacitors, flywheels, and batteries), ACAC matrix converters and high-power high-frequency DCDC and DCAC power converters oriented to electric vehicles and smart grid applications.

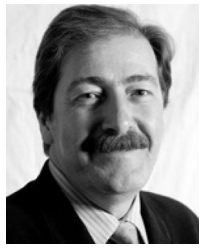

Luis Fontan (SM'05) received the Doctor of Engineering degree from the University of Navarra (UN), Spain, in 1988.

Since then, he has been working in applied research projects at CEIT and, since 1987, lecturing at the UN. He is currently a Principal Researcher and head, since 2004, of the Electronics Unit of CEIT and a Professor at the University of Navarra (UN), Spain. His main research and technical interests include the following areas: analysis, modeling and simulation of electromagnetic devices; analysis and fem modeling of conventional and no-conventional ac machines; industrial communications; power electronics; energy storage and digital signal processing for smart grids. He has been a representative of CEIT for the energy cluster, since 1997. He has participated in more than 35 research projects, some of them international collaborative projects, has directed five doctoral theses and is author or coauthor of about 30 scientific and technical publications in national and international journals and conferences.